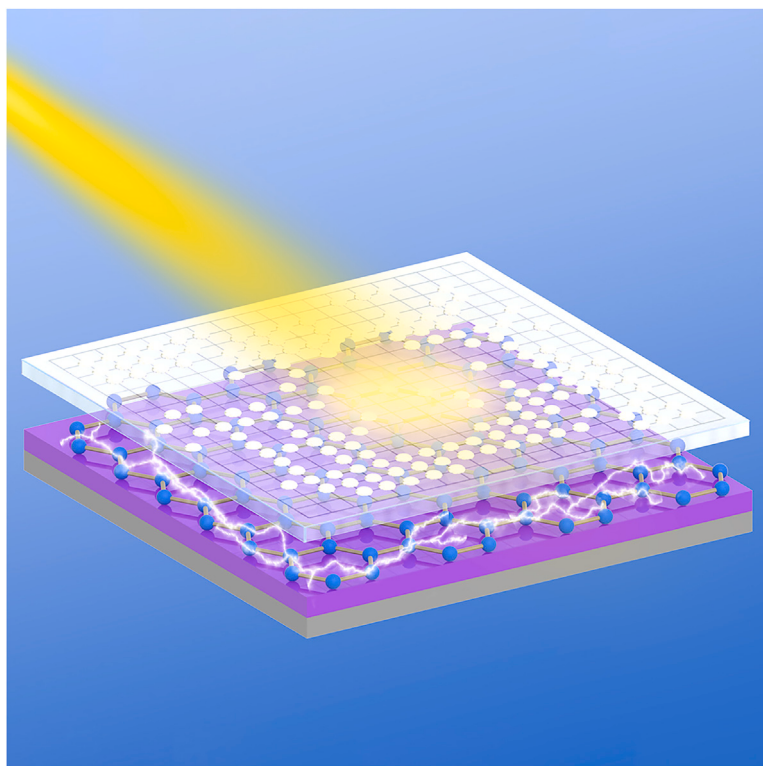


Article

Synergistic effect of graphene enhances the responsivity of hybrid perovskite photodetector



Chu et al. prepare large-area graphene and synthesize Ag-rGO to fabricate a MAPbI₃ photodetector. The synergistic effect of graphene is proven to enlarge the grain size of MAPbI₃ film and enhance the absorbance. DFT calculations and FDTD solutions also endorse the absorption enhancement of the perovskite layer and the synergistic effect.

Jingyu Chu, Zirui Liu, Peiding Liu, Jiyang Xie, Jinzhong Xiang, Feng Qiu

fengqiu@ynu.edu.cn

Highlights

MAPbI₃ perovskite films via an *in situ* hot-casting scheme

Synergistic effect of graphene enhances the absorbance of MAPbI₃

Surface plasma resonance effect enhances the photodetectors' responsivity

DFT calculation and FDTD analysis confirm the enhancement



Article

Synergistic effect of graphene enhances the responsivity of hybrid perovskite photodetector

Jingyu Chu,^{1,2} Zirui Liu,^{1,2} Peiding Liu,^{1,2} Jiyang Xie,¹ Jinzhong Xiang,¹ and Feng Qiu^{1,3,*}

SUMMARY

Organometal halide perovskite has aroused extensive interest due to its high absorption coefficient and flexible synthetic strategy for fabricating sensitive and low-cost photodetectors. Nevertheless, obtaining large and ordered orientation perovskite grain, developing enhanced optical absorption, and restraining defect states of grain boundaries are still open and challenging processes. Here, we report a flexible hierarchical architecture to promote grain growth and absorption strength. Therein, graphene and its derivatives are adopted to produce enlarged grain via an *in situ* hot-casting scheme. The surface plasmon resonance effect of highly conductive reduced graphene oxide-silver (Ag-rGO) nanoparticles is introduced to improve perovskite absorbance, enhancing responsivity by nearly four orders of magnitude to 13 AW^{-1} . Meanwhile, density functional theory calculations and finite-difference time-domain analysis confirm the absorption enhancement and effective separation of the photogenerated carriers. This work elucidates the synergistic effect of graphene based on strain template and surface plasmon resonance in fabricating high-responsivity photodetectors.

INTRODUCTION

According to the critical photoelectric mechanisms of the photovoltaic effect, photoconductive effect, photothermoelectric effect, and bolometric effect,^{1,2} photodetectors monitor the change of light signals mainly via the photocurrent effect, which responds to weak light intensity, even single photon. It has been widely applied in military detection, night vision, industrial non-destructive detection, remote sensing, and so forth.³ As a fashionable photodetector, the gain mechanisms of the photocurrent rely on fine crystal quality, high light-absorbing capacity, low interfacial trap states, and other gain architectures. Organolead triiodide perovskite is an ideal material because of its large light absorption coefficient,⁴ long carrier lifetime,⁵ and low cost.^{6,7} Up to now, the hybrid perovskite has been widely applied in the fields of solar cells,⁸ light-emitting diodes,⁹ and photodetectors.¹⁰ These robust industrializations benefit from the flexible synthetic strategies of high-quality perovskite films, such as the one-step, two-step, and anti-solvent methods. However, these methods have always existed with many unsolved problems, such as surface or grain boundary point defects, trap defects, and incompetent light absorption. To eliminate defects and harvest a high-quality hybrid perovskite film, an orderly lattice scheme, passivation strategy, and energy-efficient architectures (surface plasmon resonance [SPR] effect) are frequently applied in the preparation process. Thereinto, coordinate bonding, ionic bonding, and robust energy conversion are commonly used to deactivate the defect, passivating induced deep-level traps.^{11,12}

¹Yunnan Key Laboratory for Micro/Nano Materials & Technology, National Center for International Research on Photoelectric and Energy Materials, School of Materials and Energy, Yunnan University, Kunming 650500, China

²These authors contributed equally

³Lead contact

*Correspondence: fengqiu@ynu.edu.cn

<https://doi.org/10.1016/j.xcpr.2024.102054>



Upgrading light absorption has always been a key consideration for photodetectors. Metal nanoparticles (Ag, Au) could develop an SPR effect, increasing light absorption due to local enhancement of the electromagnetic field.^{13,14} However, hybrid perovskite photodetectors based on pure perovskites demonstrate low performance due to low carrier mobility originating from a high density of the grain boundary accompanied by abundant trap states. Hence, a light-absorbing material with high mobility was expected to be an active channel for transferring carriers, resulting in high responsivity. 2D materials are thought to be an ideal strategy to enhance the performance of photodetectors.^{15–17} As a typical healing therapy of mobility engineering, graphene has an sp^2 -hybridized hexagonal carbon atom lattice. It possesses a unique potential for electronics transport,¹⁸ which is one of the most competitive materials for being used as the channel in the photodetector. Graphene could rely on the strength of ultrahigh carrier mobility and flexible van der Waals epitaxy, contributing to the high photoelectric conversion efficiency. Graphene also facilitates crystallization and carrier separation for hybrid perovskites, further developing a high graphene/perovskite assembling detector performance.^{10,19,20}

In this paper, the single-layer graphene as an underlying graphene template is prepared via low-pressure chemical vapor deposition (CVD), and organic-inorganic hybrid perovskite MAPbI₃ is synthesized by an *in situ* one-step hot-casting method. The van der Waals epitaxial grain size of MAPbI₃ film becomes larger to approximate dozens of microns via the underlying graphene template, whose sizes are boosted over an order of magnitude compared to a conventional post-annealing strategy. Moreover, microwave-synthesized reduced graphene oxide-silver (Ag-rGO) nanoparticles are added to the precursor solution. The adhesion of the Ag atoms results in an SPR effect, which augments the photocurrent. Finally, the synergistic effect of the underlying graphene template and Ag-rGO-based SPR prominently promotes the photocurrent by four orders of magnitude. The density functional theory (DFT) calculations and finite-difference time-domain (FDTD) analysis also endorse the findings.

RESULTS AND DISCUSSION

Fabrication procedures

The graphene/MAPbI₃/Ag-rGO photodetector is fabricated as follows (Figure 1). Firstly, the large-area and high-mobility graphene was prepared via a conventional CVD method (Figures S1 and S2; Notes S1 and S2).²¹ Then, the graphene was transferred onto a hydrophilic SiO₂/n-Si substrate by wet transfer method after ultraviolet (UV)-ozone cleaning (Figure S3; Note S3). Acetone generally removes the PMMA sacrificial transfer layer to harvest clean graphene. However, acetone-treated hydrophobic graphene does not facilitate the process of perovskite crystallization. UV-ozone treatment is a conventional hydrophilia post-processing technology. However, when UV-ozone is exploited to treat the graphene, it destroys its lattice. Therefore, the hydrophilic strategy of graphene is updated to an anti-solvent of toluene, which would help crystallize the perovskite due to the hydrophilic graphene. Additionally, Ag-rGO was synthesized via a microwave strategy as an ultrahigh mobility and conductivity additive.^{22,23} After that, the Ag-rGO was added to the precursor solution. This as-synthesized Ag-rGO hybrid can accelerate carrier generation and fast extraction.²⁴ Finally, the perovskite films were *in situ* prepared by a hot-casting scheme to obtain millimeter-scale grain.²⁵ Herein, the hot plate was maintained at 100°C for spin coating, resulting in a highly oriented crystal, which would reduce trap defects and improve mobility in the perovskite. Finally, the

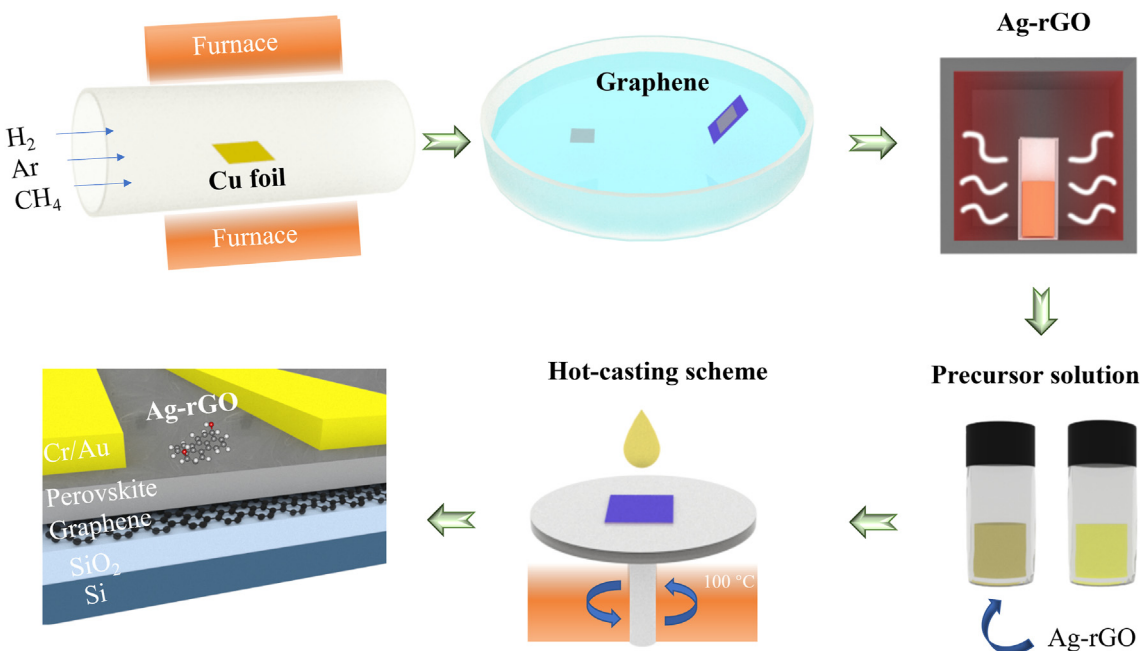


Figure 1. Schematic diagram of the fabrication procedure for the graphene/MAPbI₃/Ag-rGO photodetector

architecture of the hybrid photodetector was fabricated to be Ag-rGO/perovskite/graphene/SiO₂/n-Si.

Structural characteristics

To confirm the contribution of the underlying graphene and Ag-rGO for perovskite grain growth and assembly, the structural characteristics of the perovskite, underlying graphene, and Ag-rGO are analyzed. Herein, the cross-sectional image and surface morphology of the MAPbI₃ perovskite film show that the perovskite film with an approximately 640 nm thickness was compactly grown without a pinhole under the assistance of an underlying graphene template (Figures 2A and 2B). The D and G bands of underlying graphene are located at ~1,347 and ~1,599 cm⁻¹, and a low ratio of I_G/I_{2D} peaks proves it is a single-layer graphene. Moreover, the average size of the induced grain is increased from 2.4 to ~40 μm via perfect wettability and template induction (Figure 2C). This improved grain size is over an order of magnitude compared to a conventional post-annealing strategy. This effective template strategy²⁶ benefits from the compatible and matching atomic configuration between the tetragonal (β -phase) perovskite and hexagonal graphene. Additionally, the typical morphological features of Ag-rGO were determined by transmission electron microscopy (TEM) analysis (Figure 2D). The high-resolution TEM image of Ag-rGO gives its lattice fringe, corresponding to (111) planes of the Ag nanoparticles with an interplanar distance of 0.23 nm.²⁷ It is found that Ag nanoparticles anchoring in rGO were typically spherical, with a (111) crystallographic orientation and a Gaussian distribution with a size between 10 and 15 nm dispersed uniformly (Figure S4; Note S4).

Characteristics of perovskite film

The conformation of Ag-rGO is further investigated. Based on the X-ray photoelectron spectroscopy (XPS) element scans of C 1 s, O 1 s, Ag 3 d, and C s of Ag-rGO, the ratios of C/O in Ag-rGO and GO were calculated to be 4.57 and 3.29, respectively, indicating that the content of the O element in Ag-rGO was effectively reduced

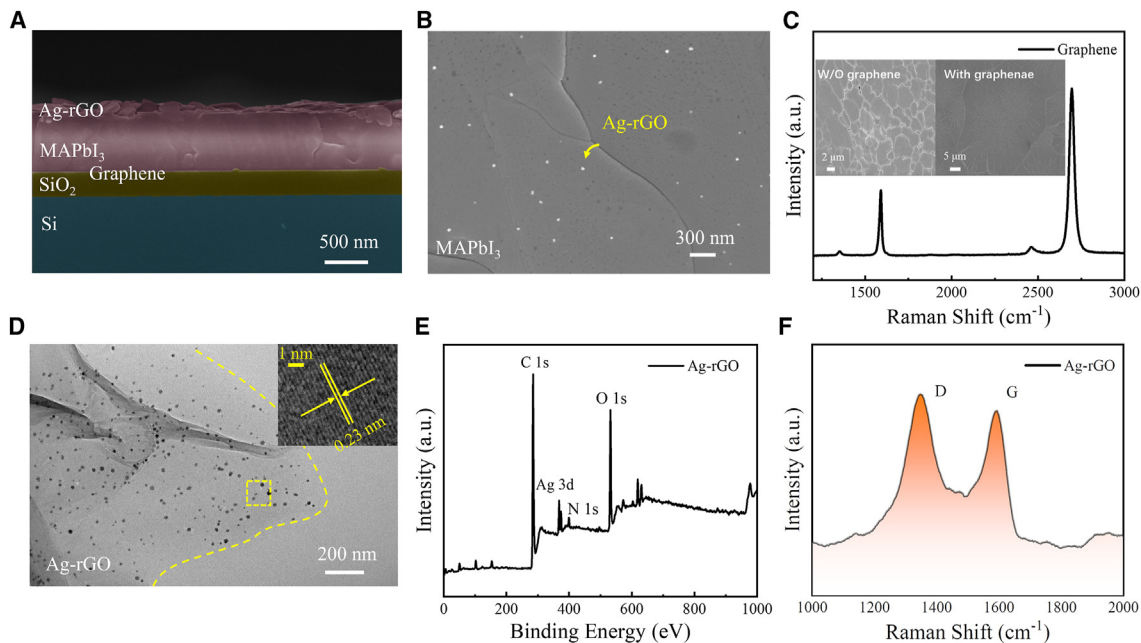


Figure 2. Structural characteristics of the Ag-rGO/MAPbI₃/graphene architecture

- (A) Cross-sectional profile of Ag-rGO/MAPbI₃/graphene architecture. Scale bar, 500 nm.
- (B) Surface morphology of perovskite grain and Ag-rGO. Scale bar, 300 nm.
- (C) Raman spectrum of underlying graphene. The inset is the surface morphology of perovskite grains without and with the underlying graphene, indicating that the graphene markedly facilitates larger grains. Inset scale bars, 2 μ m and 5 μ m.
- (D) High-resolution topological morphology of Ag-rGO on perovskite grain, including an anchoring Ag nanoparticle framework. Scale bar, 200 nm. The inset is the high-resolution TEM image of Ag crystal, indicating a lattice spacing of 0.23 nm for the <111> preferred orientation. Inset scale bar, 1 nm.
- (E and F) XPS spectrum (E) and Raman spectrum (F) of Ag-rGO, respectively.

(Figures 2E and S5). Raman spectroscopy is a sensitive method to characterize graphene and its derivatives. The Raman spectra of Ag-rGO, GO, and graphene can also be distinguishable (Figures 2F and S6; Note S5). For Ag-rGO and GO, the D and G band peaks correspond to approximately 1,350 and 1,597 cm^{-1} , respectively. The intensity ratio of I_D/I_G can identify the difference between Ag-rGO and GO, whose ratio values are about 1.02 and 0.92, indicating more defects in Ag-rGO originating from the oxygen-containing functional groups.²⁸

To obtain a large grain and insight into the perovskite crystal orientation, the film structure is analyzed via room temperature and temperature-dependent X-ray diffraction (XRD). As a typically modified spin-coating method, the *in situ* hot-casting avenue,²⁵ quasi-hot-casting approach,²⁹ or flash infrared annealing³⁰ can all produce a large and strong preferential orientation grain along the (112) directions for MAPbI₃, indicating the typical tetragonal phase. Moreover, the XRD patterns of the MAPbI₃ with or without graphene and Ag-rGO develop the specific peaks of MAPbI₃, indicating the same tetragonal crystals in Figures 3A–3C. It shows prominent peaks at $2\theta = 19.86^\circ$ and 40.48° associating with the (112) and (224) crystallographic planes, respectively. In addition, the underlying graphene, acting as a template method for crystal growth, also induces lattice shrinkage of MAPbI₃, resulting in a minor compression strain of -0.84% in the <112> preferred orientation (residual strain $\epsilon_{112} = (d_{112} - d_0)/d_0$, where d_{112} and d_0 are the strain and primitive lattice parameters, respectively^{31,32}) (Figures S7A and S7B). According to some results of strain research, this strain is also beneficial to phase stability and efficiency management.³³ To confirm the feasibility of the *in situ* hot-casting approach²⁹ and

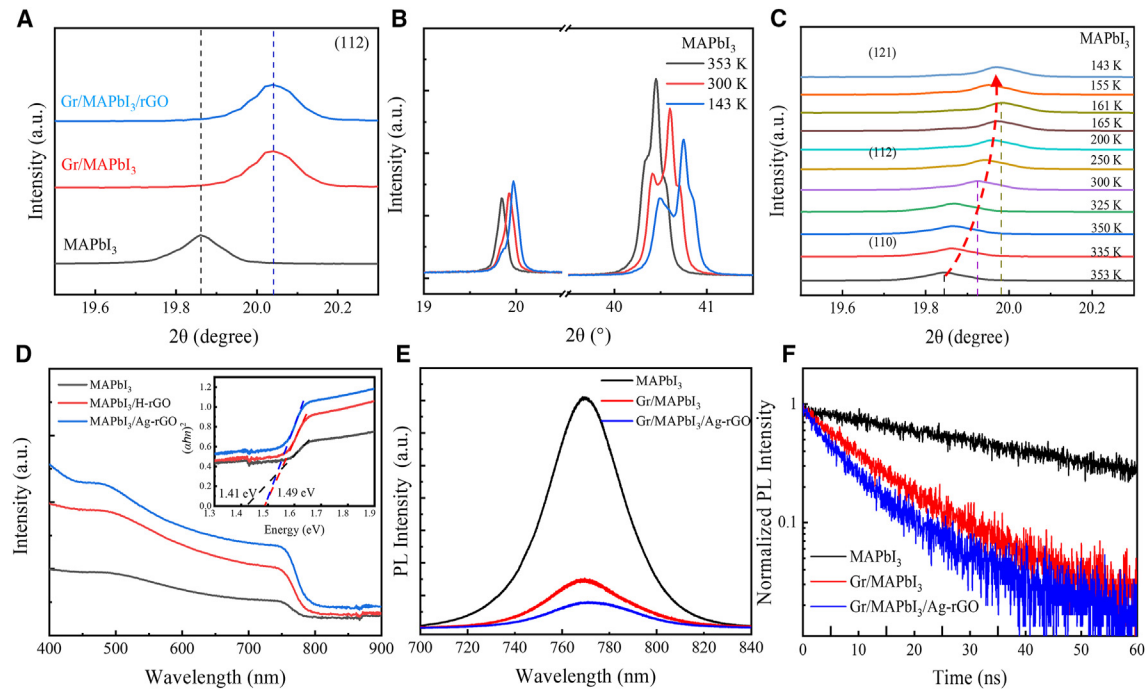


Figure 3. Graphene synergistic effect regulates the structural quality of hybrid perovskite

(A) Room temperature XRD patterns for different perovskite architectures.

(B and C) The enlarged and overall temperature-dependent XRD patterns of MAPbI₃.

(D) UV-visible absorption spectra of perovskite with optimal rGO. Inset shows the Kubelka-Munk plot of $(\alpha h\nu)^2$ versus photon energy ($h\nu$), where α is the absorption coefficient.

(E and F) Steady-state PL (E) and time-resolved PL spectra (F) for perovskite with underlying graphene or surface rGO passivation.

perovskite stability, the temperature-dependent crystal structure of the MAPbI₃ perovskite is also investigated. As reported before, the crystal phase of MAPbI₃ perovskite enables phase transitions from an orthorhombic (γ -phase) structure at 161 K to a tetragonal (β -phase) structure at room temperature and then to a cubic (α -phase) structure at 330 K.^{7,34} The phase transitions are also confirmed by the temperature-dependent XRD patterns shown in Figures 3B and 3C. With the temperature increasing, the crystallographic planes are shifted from (121), (400), and (224) at 143 K for γ -phase to (112) and (220) at 300 K for β -phase and then to (110) and (220) at 353 K for α -phase (Figures 3B and 3C). These phase transitions prepared from the hot-casting scheme are consistent with the structure of variable-temperature MAPbI₃ perovskite films via conventional spin coating.³⁵ As the temperature increases, the diffraction peak shifts to the left, resulting in tensile stress, which indicates that the material is a positive expansion coefficient material. Therefore, the underlying graphene-induced compression strain and thermal-induced tensile stress can be compensated for, resulting in less residual stress of the perovskite film. Therefore, the graphene hybrid perovskite can defend against thermal decomposition.

To obtain highly conductive rGO and efficient passivation, rGO with different preparation methods is investigated and chosen. Herein, H-rGO was synthesized by CVD at 1,000°C in a hydrogen atmosphere³⁶ without Ag nanoparticles, while the highly conductive Ag-rGO was synthesized via a microwave strategy. The UV-visible absorption spectra of the pure perovskite and perovskite/rGO hybrid samples are studied (Figure 3D). These composites increased the absorbing ability and exhibited a

slightly higher absorption edge than the perovskite. The hybrid with Ag-rGO shows a better absorbance, which would contribute to a high conductivity and plasmon resonance effect due to Ag nanoparticles in Ag-rGO.^{22,37}

To gain insight into the contribution of graphene and Ag-rGO for efficient electron-hole dissociation, transfer, and extraction, the steady-state and time-resolved photoluminescence (TRPL) spectra are investigated. Figure 3E exhibits the steady-state PL spectra of the perovskite, graphene/perovskite, and graphene/perovskite/Ag-rGO hybrid samples at room temperature. Under the same experimental conditions, the peak was located at 769.5 nm and had a little red shift to 770.6 nm when Ag-rGO was added. Moreover, there was a decrease in the PL intensity of up to nearly 80% for the hybrid perovskite. This phenomenon results from reduced defects and the effective transfer of photon-generated carriers. Therefore, the quantum yield is limited, and the transfer time of carriers is shortened, which could be supported by the TRPL decay curves (shown in Figure 3F). The PL lifetime changed from 45.0 to 7.8 ns (Table S1) when the perovskite was spun onto the graphene. The lifetime was further shortened when the Ag-rGO was added into the perovskite with a lifetime of approximately 4.4 ns. This is the direct consequence of the charge-carrier extraction across the interface of graphene and perovskite. Therefore, the effective transfer of photon-generated carriers is a critical prerequisite of high-performance detectors. Herein, the photon-generated hole in the graphene/perovskite/Ag-rGO hybrid architecture is transferred from the valence band of the perovskite to graphene. The photon-generated electron is transferred from the conduction band of the perovskite to rGO (Figure S8). Further, the high extraction efficiency and effective carrier transfer were attributed to the enlarged grain size and reduced trap density.³⁸

Calculations

To elucidate the contributions of graphene, Ag-rGO, and Ag nanoparticles to perovskite, the DFT analysis is implemented. MAPbI₃ is a β -phase configuration when the perovskite absorber is normally working. Previous work has shown that Pb in the (001) surface of MAPbI₃ is more stable as a termination surface.³⁹ Therefore, Pb atoms and the (001) surfaces of the β -phase and γ -phase MAPbI₃ are used as the termination surface to build the simplified calculation model (Figure S9). The interaction between graphene and MAPbI₃ surfaces was developed using the repeated-slab model. In order to construct a MAPbI₃/graphene heterojunction, graphene after $7 \times 2\sqrt{3}$ relaxation is used as the substrate, and then 2×1 MAPbI₃ with a (001) orientation is used to cover the graphene (Figures S10A and S10B). The vacuum separation was set to 20 Å to avoid the spurious vertical coupling effect.^{39,40} The silver dimer anchors the surface of the perovskite, and the rGO/graphene model is established based on the hanging functional group of OH in rGO via XPS characterization (Figures S10C and S10D).

To explore the band-gap changes for various perovskite configurations, two-phase perovskites of γ -MAPbI₃ and β -MAPbI₃, corresponding to the low- and room temperature structural frameworks, are built (Figure S11). This indicates that the electronic structures are both direct band gaps, and the two types are 1.79 and 1.63 eV at 77 K and room temperature, respectively. Direct band-gap semi-conductors do not require the participation of phonons in electronic transitions and have excellent photoelectric conversion efficiency. The distinction of the band gap is tiny at only 0.16 eV, indicating that it maintains good stability without an energy-level change. Additionally, the Fermi level is adjacent to the valence band top, and the

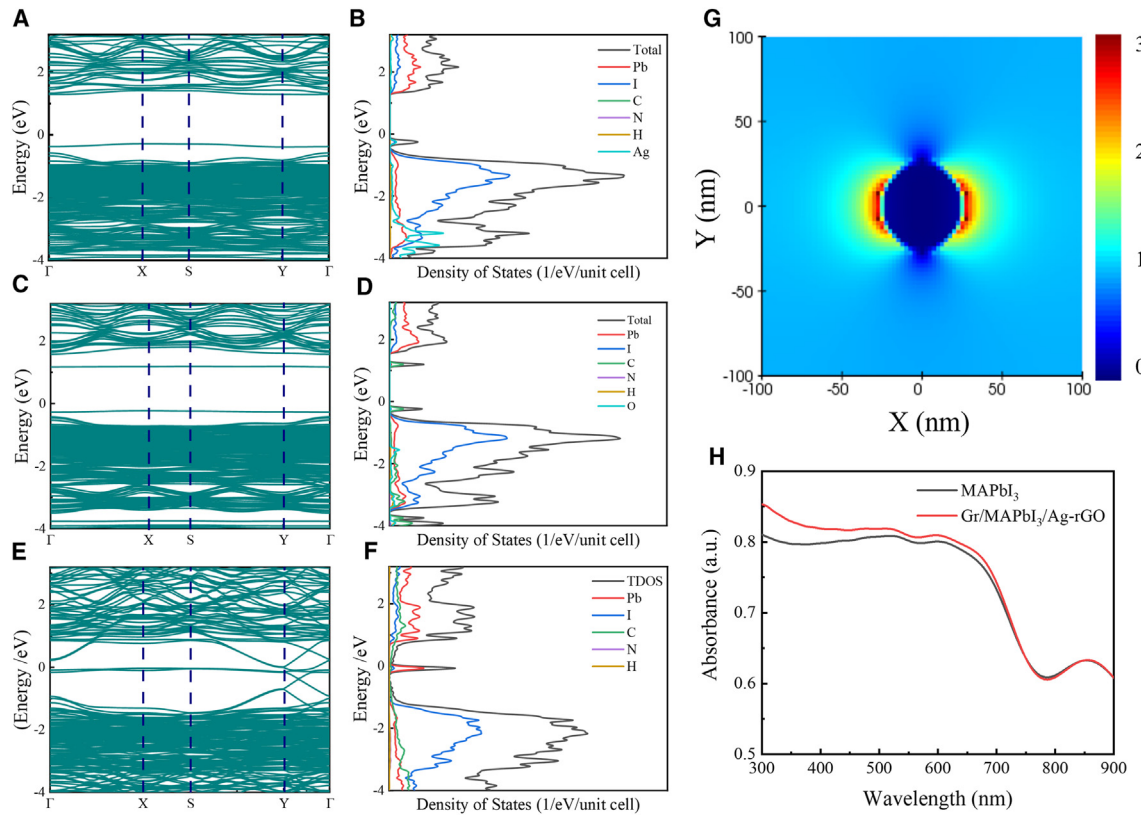


Figure 4. DFT calculations and FDTD analysis

(A and B) Energy band structures (A) and density of states (DOS) (B) for silver dimer loaded on β -phase MAPbI₃ (001).

(C and D) Energy band structures (C) and DOS (D) for rGO adsorbed on β -phase MAPbI₃ (001).

(E and F) Energy band structures (E) and DOS (F) for β -phase MAPbI₃/graphene.

(G) The electric field of Ag-rGO.

(H) Absorbance spectra of the structure of the MAPbI₃ and graphene/MAPbI₃/Ag-rGO simulated by FDTD Solution.

bottom of the conduction band and the top of the valence band are contributed by the Pb and I elements, respectively.⁴¹

After that, the energy band and density of states of the heterojunction constructed by the perovskite-loaded silver dimer, rGO adsorbed on the perovskite, and perovskite assembled on the graphene were calculated. After adding Ag-rGO to the perovskite, the response performance of the photodetector has been significantly improved. To explore the reasons for the improved photoelectric performance, the band structure, density of states, and differential charge density of rGO with small molecules and silver dimers anchored on the surface of perovskite are calculated (Figures 4A and 4B). The silver load on the perovskite produces a plasma effect to promote the light absorption of the perovskite. The loading of the silver dimer causes the top of the valence band to move up. This is because the silver dimer's charge transfer occurs on the perovskite's surface, and then the coupling occurs. The charge in the silver dimer is transferred to the perovskite so that the concentration of carriers in the perovskite can be increased, resulting in improved photoelectric performance. After adding rGO molecules, the energy band structure shows that the conduction band shifts downwards and the valence band tops shift upwards, which helps to reduce the stimulated energy for electronic transitions (Figures 4C

and 4D). Moreover, adding graphene can inject electrons into the perovskite, increasing the carrier concentration (Figures 4E, 4F, and S13D).

Single-layer graphene has semi-metallic properties with zero band gap. The properties of the semi-metallic graphene promote the transport of electrons (Figure S12). It can also be seen that graphene mainly contributes to energy-level occupation near the Fermi level of the perovskite/graphene heterojunction. To explore the charge transfer between the perovskite/graphene heterojunction, the differential charge density was calculated. It clearly shows the accumulation and depletion of charge between the γ -phase and β -phase perovskites with graphene (Figures S13C and S13D; Note S6). At the interface, the charge in graphene is extracted to the perovskite, the graphene accumulates more positive charges, and the perovskite accumulates more electrons. Such interface charge distribution can effectively promote charge transport. Due to the asymmetry of the charge distribution at the interface, a built-in electric field is formed, which can effectively separate photogenerated electrons and holes and inhibit their recombination.

The software FDTD Solutions (Lumerical) was used to calculate the electric field (Figure 4G). It shows the FDTD simulation and the electric field distribution on the surface of Ag-rGO-anchored MAPbI₃. In this case, a light source with a wavelength ranging from 300 to 900 nm was placed on top of the device. To simplify the calculation, the material properties of Si/SiO₂/graphene/MAPbI₃/Ag-rGO were used for the simulation. The total simulation window was 200 × 200 nm, and the mesh sizes were set to 2 × 2 × 2 nm. As a result, the absorbance has an apparent increase due to the enhanced local electric field. (Figure 4H).

Performance

To achieve an insight into the photoelectric response, the current was measured at different illumination powers under vacuum and room temperature. The photocurrent increased when the irradiance changed from 0.93 to 4,650 mW/cm² (shown in Figures 5A–5C). When graphene and Ag-rGO were added, the current reached several milliamperes in the graphene/perovskite hybrid photodetector device with Ag-rGO. Additionally, the speed of the photoresponse of our devices is fast, with the rise and fall times of the perovskite photodetector measured to be about 8.5 and 16.3 ms, respectively, under a bias voltage of 0.1 V when the irradiance is 465 mW/cm² (Figure 5D), revealing its ultrafast photoresponse rate. The rise and fall times decreased to 39.8 and 25.2 ms, respectively, in the graphene/perovskite hybrid photodetector (Figures 5E and 5F). With Ag-rGO added, the rise and fall times were 207 and 335 ms, respectively. The response speed is not regulated flexibly via the graphene strategy, which is limited by the resistance-capacitance time constant, unpassivated surface defects, and thick bulk crystals.^{2,42}

The pure perovskite photodetector does not have a remarkable gain with a low responsivity of about 10⁻³ AW⁻¹. When graphene was added, the responsivity of the device increased slightly but exhibited good on-off switching behavior (Figure 5G). However, once decorated with Ag-rGO, the responsivity of the hybrid photodetector reached 13.19 AW⁻¹, which is increased by nearly four orders of magnitude and is comparable with that of high-quality MAPbI₃ detectors.^{19,20}

The noise power spectra ($S_n(f)$) of a typical device with or without graphene and its derivative are analyzed using a noise characterization system in ambient

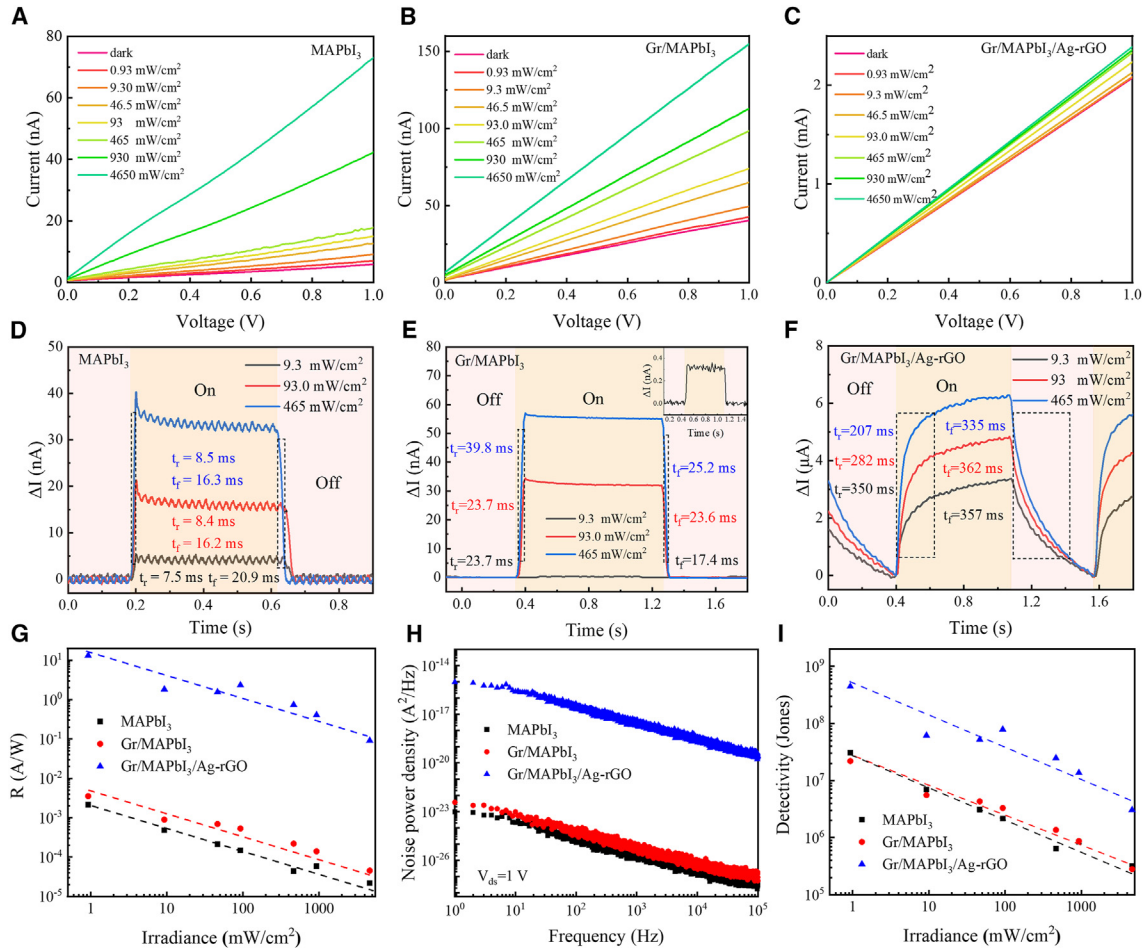


Figure 5. Optoelectronic response of MAPbI₃/graphene/Ag-rGO photodetectors

Current-voltage curves and time response of the device illuminated with and without a 532 nm laser irradiation at a voltage of 0.1 V under different irradiation power intensities.

(A and D) Current-voltage curves (A) and time response (D) of MAPbI₃ photodetectors illuminated with and without a 532 nm laser irradiation at a voltage of 0.1 V under different irradiation power intensities.

(B and E) Current-voltage curves (B) and time response (D) of graphene/MAPbI₃ photodetectors illuminated with and without a 532 nm laser irradiation at a voltage of 0.1 V under different irradiation power intensities.

(C and F) Current-voltage curves (C) and time response (F) of graphene/MAPbI₃/Ag-rGO photodetectors illuminated with and without a 532 nm laser irradiation at a voltage of 0.1 V under different irradiation power intensities.

(G–I) The responsivity (G), spectra of noise power density (H), and specific detectivity (I) of graphene-based MAPbI₃ detectors.

conditions.⁴³ The sample was encapsulated in a metal box to be shielded from environmental noises. Figure 5H displays the spectra of the current noise power density of the device plotted in double logarithmic coordinates. All of the curves exhibit a clear characteristic flicker (1/f type) noise. The calculated D^* of the device by 1/f noise is shown in Figure S14 and Note S7. However, due to the possible leakage current originating from large-area Ag-rGO in the surface of grain boundaries, the flicker noise-limited specific detectivity (D^*) is not improved. Therefore, the critical D^* would be appealed to the shot-noise-limited detectivity and can be calculated from the following equation⁴³:

$$D^* = \frac{R}{(2qI_d/A)^{1/2}} \quad (\text{Equation 1})$$

where q is the elementary charge, I_d is the dark current, and A is the area of the device. For our device, $A = 7.5 \times 10^{-5} \text{ cm}^2$. Based on assembled graphene engineering, the D^* is elevated over one order of magnitude up to $5.0 \times 10^9 \text{ Jones}$ (Figure 5*I*). By virtue of the strain template and SPR, this synergistic graphene effect has been demonstrated to be effective in boosting the detector's photoresponse and detection capability.

In summary, the crystal orientation of a (112) hybrid perovskite is prepared via an *in situ* hot-casting scheme, which could yield a larger grain for MAPbI₃ with alleviated strain and reduced interfacial defects. The effect of graphene and its derivatives Ag-rGO by graphene engineering results in strain template and surface plasmon absorption. Herein, the high mobility of graphene is conducive to transfer carriers, and Ag atoms generate an SPR effect to enhance electric field and light absorption. Then, a cheap and straightforward method for flexible graphene/perovskite hybrid photodetectors is successfully fabricated. These devices demonstrate an outstanding photoresponsivity, higher than that of pure perovskite photodetectors by nearly four orders of magnitude, as well as an elevated detection capability over one order of magnitude. Finally, this synergetic effect of graphene is significant for fabricating high-performance photodetectors.

EXPERIMENTAL PROCEDURES

Resource availability

Lead contact

Further information should be directed to the lead contact, Feng Qiu (fengqiu@ynu.edu.cn).

Materials availability

This study did not generate new unique materials.

Data and code availability

Any additional information required to reanalyze the data reported in this paper is available from the lead contact upon request.

Characterization and measurements

The crystalline phase structures of the films were examined by XRD with Cu K α radiation (Rigaku Smartlab SE). Raman spectra were implemented by a confocal Raman with a 532 nm excitation laser (1 mW) (HORIBA LabRAM HR Evolution). UV-visible spectra were obtained using Shimadzu UV-3600. The morphology and microstructure of the films were examined by field-emission scanning electron microscopy (Zeiss Gemini 500) and energy dispersion spectroscopy (Oxford Ultimate MAX40). TEM (JEM-2100) was used to investigate the structure and morphology of the Ag-rGO. The PL and TRPL spectra were obtained by FLS1000 (Edinburgh). The valence states were analyzed via XPS using a monochromatic Al K α radiation source (Thermo Fisher Escalab 250Xi). Electrical transport, noise measurement (1 Hz–100 kHz), and photoresponse measurements were performed using a semi-conductor parameter tester (FS-Pro, Primarius Technologies). The incident laser was attenuated using various neutral-density filters and controlled using an aperture (aperture diameter = 1,016 μm). The laser powers were recorded using a power meter (Thorlabs PM100D), producing light power intensities (=power/aperture area).

Other detail methods are outlined in the [supplemental experimental procedures](#).

SUPPLEMENTAL INFORMATION

Supplemental information can be found online at <https://doi.org/10.1016/j.xcpr.2024.102054>.

ACKNOWLEDGMENTS

This work was supported by the National Natural Science Foundation of China (nos. 12064047 and 11864044), the Key and General Program of Yunnan Fundamental Research Projects (nos. 202201AS070010 and 202001BB050051), and the Major Special Project of Yunnan Science and Technology Program (no. 202202AB080019).

AUTHOR CONTRIBUTIONS

Conceptualization, J.C., Z.L., and P.L.; methodology, J.C., Z.L., and P.L.; investigation, J.C., Z.L., and P.L.; writing – original draft, J.C., Z.L., and P.L.; writing – review & editing, F.Q.; funding acquisition, J. Xie, J. Xiang, and F.Q.; resources, J. Xie and F.Q.; supervision, F.Q.

DECLARATION OF INTERESTS

The authors declare no competing interests.

Received: January 24, 2024

Revised: April 12, 2024

Accepted: May 23, 2024

Published: June 12, 2024

REFERENCES

1. Long, M., Wang, P., Fang, H., and Hu, W. (2019). Progress, Challenges, and Opportunities for 2D Material Based Photodetectors. *Adv. Funct. Mater.* 29, 1803807. <https://doi.org/10.1002/adfm.201803807>.
2. Wang, F., Zhang, T., Xie, R., Wang, Z., and Hu, W. (2023). How to characterize figures of merit of two-dimensional photodetectors. *Nat. Commun.* 14, 2224. <https://doi.org/10.1038/s41467-023-37635-1>.
3. Hu, T., Zhang, R., Li, J.-P., Cao, J.Y., and Qiu, F. (2022). Photodetectors based on two-dimensional MoS₂ and its assembled heterostructures. *Chip* 1, 100017. <https://doi.org/10.1016/j.chip.2022.100017>.
4. Fang, Y., Dong, Q., Shao, Y., Yuan, Y., and Huang, J. (2015). Highly narrowband perovskite single-crystal photodetectors enabled by surface-charge recombination. *Nat. Photonics* 9, 679–686. <https://doi.org/10.1038/nphoton.2015.156>.
5. Wehrenfennig, C., Eperon, G.E., Johnston, M.B., Snaith, H.J., and Herz, L.M. (2014). High Charge Carrier Mobilities and Lifetimes in Organolead Trihalide Perovskites. *Adv. Mater.* 26, 1584–1589. <https://doi.org/10.1002/adma.201305172>.
6. Green, M.A., Ho-Baillie, A., and Snaith, H.J. (2014). The emergence of perovskite solar cells. *Nat. Photonics* 8, 506–514. <https://doi.org/10.1038/nphoton.2014.134>.
7. Qiu, F., Chu, J., Liu, Z., Xiang, J., Yang, J., and Wang, C. (2020). Insight into the Origins of Figures of Merit and Design Strategies for Organic/Inorganic Lead-Halide Perovskite Solar Cells. *Sol. RRL* 4, 2000452. <https://doi.org/10.1002/solr.202000452>.
8. Saliba, M., Matsui, T., Domanski, K., Seo, J.-Y., Ummadisingu, A., Zakeeruddin, S.M., Correa-Baena, J.-P., Tress, W.R., Abate, A., Hagfeldt, A., and Grätzel, M. (2016). Incorporation of rubidium cations into perovskite solar cells improves photovoltaic performance. *Science* 354, 206–209. <https://doi.org/10.1126/science.aaa5557>.
9. Lin, K., Xing, J., Quan, L.N., de Arquer, F.P.G., Gong, X., Lu, J., Xie, L., Zhao, W., Zhang, D., Yan, C., et al. (2018). Perovskite light-emitting diodes with external quantum efficiency exceeding 20 per cent. *Nature* 562, 245–248. <https://doi.org/10.1038/s41586-018-0575-3>.
10. Sun, Z., Aigouy, L., and Chen, Z. (2016). Plasmonic-enhanced perovskite–graphene hybrid photodetectors. *Nanoscale* 8, 7377–7383. <https://doi.org/10.1039/C5NR08677A>.
11. Chen, B., Rudd, P.N., Yang, S., Yuan, Y., and Huang, J. (2019). Imperfections and their passivation in halide perovskite solar cells. *Chem. Soc. Rev.* 48, 3842–3867. <https://doi.org/10.1039/C8CS00853A>.
12. Li, Y., Zhang, Y., Li, T., Li, M., Chen, Z., Li, Q., Zhao, H., Sheng, Q., Shi, W., and Yao, J. (2020). Ultrabroadband, Ultraviolet to Terahertz, and High Sensitivity CH₃NH₃PbI₃ Perovskite Photodetectors. *Nano Lett.* 20, 5646–5654. <https://doi.org/10.1021/acs.nanolett.0c00082>.
13. Atwater, H.A., and Polman, A. (2010). Plasmonics for improved photovoltaic devices. *Nat. Mater.* 9, 205–213. <https://doi.org/10.1038/nmat2629>.
14. Mubeen, S., Lee, J., Singh, N., Krämer, S., Stucky, G.D., and Moskovits, M. (2013). An autonomous photosynthetic device in which all charge carriers derive from surface plasmons. *Nat. Nanotechnol.* 8, 247–251. <https://doi.org/10.1038/nnano.2013.18>.
15. Chen, Y., Wang, Y., Wang, Z., Gu, Y., Ye, Y., Chai, X., Ye, J., Chen, Y., Xie, R., Zhou, Y., et al. (2021). Unipolar barrier photodetectors based on van der Waals heterostructures. *Nat. Electron.* 4, 357–363. <https://doi.org/10.1038/s41928-021-00586-w>.
16. Wu, F., Li, Q., Wang, P., Xia, H., Wang, Z., Wang, Y., Luo, M., Chen, L., Chen, F., Miao, J., et al. (2019). High efficiency and fast van der Waals hetero-photodiodes with a unilateral depletion region. *Nat. Commun.* 10, 4663. <https://doi.org/10.1038/s41467-019-12707-3>.
17. Tong, L., Peng, Z., Lin, R., Li, Z., Wang, Y., Huang, X., Xue, K.-H., Xu, H., Liu, F., Xia, H., et al. (2021). 2D materials-based homogeneous transistor-memory architecture for neuromorphic hardware. *Science* 373, 1353–1358. <https://doi.org/10.1126/science.abg3161>.
18. Lin, L., Zhang, J., Su, H., Li, J., Sun, L., Wang, Z., Xu, F., Liu, C., Lopatin, S., Zhu, Y., et al. (2019). Towards super-clean graphene. *Nat. Commun.* 10, 1912. <https://doi.org/10.1038/s41467-019-09565-4>.

19. Dong, R., Fang, Y., Chae, J., Dai, J., Xiao, Z., Dong, Q., Yuan, Y., Centrone, A., Zeng, X.C., and Huang, J. (2015). High-Gain and Low-Driving-Voltage Photodetectors Based on Organolead Triiodide Perovskites. *Adv. Mater.* 27, 1912–1918. <https://doi.org/10.1002/adma.201405116>.
20. Lee, Y., Kwon, J., Hwang, E., Ra, C.-H., Yoo, W.J., Ahn, J.-H., Park, J.H., and Cho, J.H. (2015). High-Performance Perovskite–Graphene Hybrid Photodetector. *Adv. Mater.* 27, 41–46. <https://doi.org/10.1002/adma.201402271>.
21. Bartelt, N.C., and McCarty, K.F. (2012). Graphene growth on metal surfaces. *MRS Bull.* 37, 1158–1165. <https://doi.org/10.1557/mrs.2012.237>.
22. Mahmoudi, T., Seo, S., Yang, H.-Y., Rho, W.-Y., Wang, Y., and Hahn, Y.-B. (2016). Efficient bulk heterojunction hybrid solar cells with graphene–silver nanoparticles composite synthesized by microwave-assisted reduction. *Nano Energy* 28, 179–187. <https://doi.org/10.1016/j.nanoen.2016.08.018>.
23. Mahmoudi, T., Wang, Y., and Hahn, Y.-B. (2019). Stability Enhancement in Perovskite Solar Cells with Perovskite/Silver–Graphene Composites in the Active Layer. *ACS Energy Lett.* 4, 235–241. <https://doi.org/10.1021/acsenergylett.8b02201>.
24. Furube, A., and Hashimoto, S. (2017). Insight into plasmonic hot-electron transfer and plasmon molecular drive: new dimensions in energy conversion and nanofabrication. *NPG Asia Mater.* 9, 454. <https://doi.org/10.1038/am.2017.191>.
25. Nie, W., Tsai, H., Asadpour, R., Blancon, J.-C., Neukirch, A.J., Gupta, G., Crochet, J.J., Chhowalla, M., Tretiak, S., Alam, M.A., et al. (2015). Solar cells. High-efficiency solution-processed perovskite solar cells with millimeter-scale grains. *Science* 347, 522–525. <https://doi.org/10.1126/science.aaa0472>.
26. Feng, J., Gong, C., Gao, H., Wen, W., Gong, Y., Jiang, X., Zhang, B., Wu, Y., Wu, Y., Fu, H., et al. (2018). Single-crystalline layered metal-halide perovskite nanowires for ultrasensitive photodetectors. *Nat. Electron.* 1, 404–410. <https://doi.org/10.1038/s41928-018-0101-5>.
27. Kumar, A., Sadanandhan, A.M., and Jain, S.L. (2019). Silver doped reduced graphene oxide as a promising plasmonic photocatalyst for oxidative coupling of benzylamines under visible light irradiation. *New J. Chem.* 43, 9116–9122. <https://doi.org/10.1039/C9NJ00852G>.
28. Li, X., Xie, H., and Mao, J. (2020). Ag nanoparticles-reduced graphene oxide hybrid: an efficient electrocatalyst for artificial N_2 fixation to NH_3 at ambient conditions. *J. Mater. Sci.* 55, 5203–5210. <https://doi.org/10.1007/s10853-020-04371-6>.
29. Wu, G., Li, X., Zhou, J., Zhang, J., Zhang, X., Leng, X., Wang, P., Chen, M., Zhang, D., Zhao, K., et al. (2019). Fine Multi-Phase Alignments in 2D Perovskite Solar Cells with Efficiency over 17% via Slow Post-Annealing. *Adv. Mater.* 31, 1903889. <https://doi.org/10.1002/adma.201903889>.
30. Muscarella, L.A., Hutter, E.M., Sanchez, S., Dieleman, C.D., Savenije, T.J., Hagfeldt, A., Saliba, M., and Ehrler, B. (2019). Crystal Orientation and Grain Size: Do They Determine Optoelectronic Properties of MAPbI_3 Perovskite? *J. Phys. Chem. Lett.* 10, 6010–6018. <https://doi.org/10.1021/acs.jpclett.9b02757>.
31. Kim, H.-S., and Park, N.-G. (2020). Importance of tailoring lattice strain in halide perovskite crystals. *NPG Asia Mater.* 12, 78. <https://doi.org/10.1038/s41427-020-00265-w>.
32. Dolabella, S., Borzi, A., Dommann, A., and Neels, A. (2022). Lattice Strain and Defects Analysis in Nanostructured Semiconductor Materials and Devices by High-Resolution X-Ray Diffraction: Theoretical and Practical Aspects. *Small Methods* 6, 2100932. <https://doi.org/10.1002/smtd.202100932>.
33. Tsai, H., Asadpour, R., Blancon, J.-C., Stoumpos, C.C., Durand, O., Strzalka, J.W., Chen, B., Verduzco, R., Ajayan, P.M., Tretiak, S., et al. (2018). Light-induced lattice expansion leads to high-efficiency perovskite solar cells. *Science* 360, 67–70. <https://doi.org/10.1126/science.aap8671>.
34. Harwell, J.R., Payne, J.L., Sajjad, M.T., Heutz, F.J.L., Dawson, D.M., Whitfield, P.S., Irvine, J.T.S., Samuel, I.D.W., and Carpenter, M.A. (2018). Role of lattice distortion and A site cation in the phase transitions of methylammonium lead halide perovskites. *Phys. Rev. Mater.* 2, 065404. <https://doi.org/10.1103/PhysRevMaterials.2.065404>.
35. Baikie, T., Fang, Y., Kadro, J.M., Schreyer, M., Wei, F., Mhaisalkar, S.G., Graetzel, M., and White, T.J. (2013). Synthesis and crystal chemistry of the hybrid perovskite $\text{CH}_3\text{NH}_3\text{PbI}_3$ for solid-state sensitised solar cell applications. *J. Mater. Chem. A* 1, 5628–5641. <https://doi.org/10.1039/C3TA10518K>.
36. Wang, S., Ang, P.K., Wang, Z., Tang, A.L.L., Thong, J.T.L., and Loh, K.P. (2010). High Mobility, Printable, and Solution-Processed Graphene Electronics. *Nano Lett.* 10, 92–98. <https://doi.org/10.1021/nl9028736>.
37. Linic, S., Christopher, P., and Ingram, D.B. (2011). Plasmonic-metal nanostructures for efficient conversion of solar to chemical energy. *Nat. Mater.* 10, 911–921. <https://doi.org/10.1038/nmat3151>.
38. Zhao, D., Sexton, M., Park, H.-Y., Baure, G., Nino, J.C., and So, F. (2015). High-Efficiency Solution-Processed Planar Perovskite Solar Cells with a Polymer Hole Transport Layer. *Adv. Energy Mater.* 5, 1401855. <https://doi.org/10.1002/aenm.201401855>.
39. Hu, J., Ma, X., Duan, W., Liu, Z., Liu, T., Lv, H., Huang, C., Miao, L., and Jiang, J. (2020). First-Principles Calculations of Graphene-Coated $\text{CH}_3\text{NH}_3\text{PbI}_3$ toward Stable Perovskite Solar Cells in Humid Environments. *ACS Appl. Nano Mater.* 3, 7704–7712. <https://doi.org/10.1021/acsanm.0c01301>.
40. Feng, J., and Xiao, B. (2014). Crystal Structures, Optical Properties, and Effective Mass Tensors of $\text{CH}_3\text{NH}_3\text{PbX}_3$ ($X = \text{I}$ and Br) Phases Predicted from HSE06. *J. Phys. Chem. Lett.* 5, 1278–1282. <https://doi.org/10.1021/jz500480m>.
41. Chen, S., Wu, C., Han, B., Liu, Z., Mi, Z., Hao, W., Zhao, J., Wang, X., Zhang, Q., Liu, K., et al. (2021). Atomic-scale imaging of $\text{CH}_3\text{NH}_3\text{PbI}_3$ structure and its decomposition pathway. *Nat. Commun.* 12, 5516. <https://doi.org/10.1038/s41467-021-25832-9>.
42. Bao, C., Chen, Z., Fang, Y., Wei, H., Deng, Y., Xiao, X., Li, L., and Huang, J. (2017). Low-Noise and Large-Linearity-Dynamic-Range Photodetectors Based on Hybrid-Perovskite Thin-Single-Crystals. *Adv. Mater.* 29, 1703209. <https://doi.org/10.1002/adma.201703209>.
43. Zhang, W., Qiu, F., Li, Y., Zhang, R., Liu, H., Li, L., Xie, J., and Hu, W. (2021). Lattice Defect Engineering Enables Performance-Enhanced MoS_2 Photodetection through a Paraelectric BaTiO_3 Dielectric. *ACS Nano* 15, 13370–13379. <https://doi.org/10.1021/acsnano.1c03402>.